Aachen Institute for Advanced Study in Computational Engineering Science

Preprint: AICES-2010/08-03

31/August/2010

Experimental and Numerical Analysis of an Hypersonic Compression Corner for Testing the Prediction Capability of a Reynolds Stress Model

A. Bosco, L. Brown B. Reinartz and R. Boyce

RWTH AACHEN UNIVERSITY

AICES

Financial support from the Deutsche Forschungsgemeinschaft (German Research Association) through grant GSC 111 is gratefully acknowledged.

List of AICES technical reports: http://www.aices.rwth-aachen.de/preprints

EXPERIMENTAL AND NUMERICAL ANALYSIS OF AN HYPERSONIC COMPRESSION CORNER FOR TESTING THE PREDICTION CAPABILITY OF A REYNOLDS STRESS MODEL

A. Bosco[1], *L. Brown*[2] *B. Reinartz*[3] *and R. Boyce*[4]

[1] *Aachen Institute for Advanced Study in Computational Engineering Science, RWTH Aachen (Germany)*
[2] *University of New South Wales at the Australian Defence Force Academy (Australia)*
[3] *Chair for Computational Analysis of Technical Systems, RWTH Aachen (Germany)*
[4] *Centre for Hypersonic, The University of Queensland (Australia)*

bosco@aices.rwth-aachen.de

Abstract

The use of second order closure models for the study of complex flows, like hypersonic flows, has not been widely investigated both because of the numerical stiffness and the decreased numerical robustness. In this work we aim to compare the numerical results obtained with a Reynolds Stress Model and experimental results from a shock tunnel to judge the prediction capability of a 7-equation turbulence model. In addition results of a two equation model like the SST k-ω model will be used as a base-line for Boussinesq-based turbulence model. Particularly we are interested in two configurations: a 15 degree compression corner that generates attached turbulent flow and a 40 degree compression corner that generates a separated turbulent flow. Preliminary results on the 40 degrees corner are presented here.

1 Introduction

Currently the majority of the codes employed in design studies of hypersonic vehicles relies on one- and two- equations turbulence models based on the Boussinesq hypothesis for the prediction of turbulent flow as reported by Roy et al. (2006) and Olsen et al. (2005). However, for wall dominated flows with thick boundary later, strong shock/boundary-layers interaction and with separation, as they are of interest here, the assumption of a linear dependence between the Reynolds stress tensor and the strain rate tensor is not always valid. Nevertheless the use of advanced turbulence models such as Reynolds Stress Models (RSM) is limited because of the computational effort required and their intrinsic reduction of numerical stability. The advantages of second order models are that they naturally include effects of streamline curvature and rotation and they resolve normal stress anisotropy close to solid walls. For these reasons a Reynolds Stress Model has been implemented and is being used in the QUADFLOW solver and being used for hypersonic inlet simulations. The results obtained in Bosco et al. (2009) show the capability of the model to correctly predict the shocks position, the boundary layer separation and the shock reflections in a scramjet intake along the central line where experimental results are available for comparison. However no significant improvement has been noticed moving from a two- to a 7-equations model. For these reasons an experimental campaign has been initiated to collect data in significant flow regions (separation region, bubble and reattachment region) where anisotropic and three-dimensional effects are more likely to occur. The results obtained will be compared with two-dimensional and three-dimensional numerical computations.

2 Experimental Campaign

T4 Shock Tunnel

The experiment is performed in the T4 free-piston tunnel at the University of Queensland (Mee (2002)).

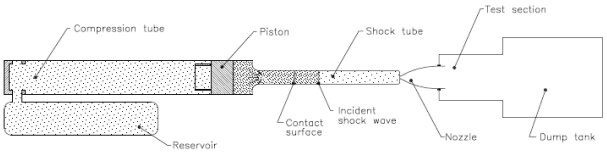

Figure 1: Schematic of the T4 shock tube as from Smith (1999).

The T4 shock-tunnel, shown in Figure 3 consist of four main sections: a high-pressure reservoir, a compression tube, a shock tube and a test section. When the tunnel is fired a piston is driven by the high pres-

sure air coming from the reservoir, through the compression tube. At the end of the compression tube a metal-diaphragm breaks once a sufficient pressure is reached. At this moment a shock wave is generated in the test gas inside the shock tube and a contact surface separates the driver gas from the test gas. Once the shock wave reaches the end of the shock tube it is reflected in the compression tube and traveling backwards it stagnates the test gas. The test gas breaks a thin secondary diaphragm and finally enters the test section. The unsteady nozzle process can now start and be followed by a steady established flow. A Mach 6.68, axisymmetric, contoured nozzle is used. Experiments are performed using air as test gas, a nozzle-supplied enthalpy of about 3MJ/kg and a unit Reynolds number of about 10x10^6 m^{-1}. The tunnel, under this operational conditions, provides approximately 2 ms of test time. The gauges used in the experiment sample the flow every microsecond.

Model design

The model design is shown in figure 2. The flat plate and the ramp are 150 mm and 250 mm long, respectively. The model is 150 mm wide. A boundary layer trip is used to enhance laminar to turbulent transition. It consists of triangular elements positioned 50 mm from the leading edge. The ramp angles investigated here are 15 degree, which should provide a turbulent attached flow and 40 degrees that has been proved to provide a turbulent separated flow. Flush-mounted thin film gauges (TFG) are used to measure the heat fluxes on the flat plate and k-type thermocouples are used to measure them along the compression ramp. 10 Kulite pressure sensors are distributed along the model for pressure measurements. The TFG are located in the separation region and are divided in two groups of 12 gauges. Each group consists of 12 sensors distributed as a cross, 8 in the flow direction and 4 in the cross flow direction. In the first group the 8 gauges in the flow direction are placed along the center line. The gauges belonging to the second group are placed 56.85 mm away from the center line. The thermocouples are placed in the reattachment region and distributed in 4 rows of 8 gauges. The gauges of two adjacent rows are slightly displaced. Additionally 6 gauges have been placed along the center line. The unusual distribution of the heat transfer gauges along the model has been chosen to allow heat transfer measurement in the cross flow and discover possible three-dimensional effect in the separation bubble as well as at the reattachment.

STN code

The nozzle exit conditions are estimated using a software called STN (Shock Tube and Nozzle Calculations for Equilibrium Air), from Krek et al. (1993), which calculates the flow properties in a reflected shock tunnel. This can be done providing the initial shock tube fill pressure, the initial temperature of the test gas in the shock tube, the incident shock speed, the measured nozzle supply stagnation pressure, the flow conditions at the nozzle throat and the flow conditions at the nozzle exit.

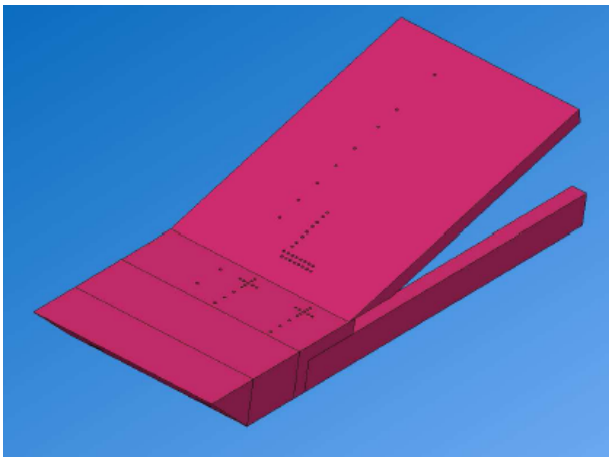

Figure 2: Schematic of the experimental model.

Pitot survey

The conical nozzle used for the campaign generates a core flow of almost uniform flow which is bounded by the expansion waves that propagate at the edges at the nozzle itself. A pitot pressure survey has been conducted at the end of the test campaign to assess the non-uniformities of the freestream flow, to prove the repeatability of the conditions between different shots and to determine the appropriate pitot-to-nozzle-supply pressure ratio (p_p/p_s) to be used for post processing the results.
The pitot rake, consisting of 33 PCBs piezoelectric pressure transducers, has been located 33 mm away form the nozzle exit which corresponds to a position 80 mm downstream of the plate leading edge for the considered model. Considering the limited extension of the model in the flow direction only one location of the rake has been investigated but measurements have been taken for two vertical position to increase the spatial resolution.

3 Numerical Analysis

QUADFLOW Solver

QUADFLOW solves the Euler and Navier-Stokes equations around complex aerodynamic configurations (Bramkamp et al (2004)). It uses a cell-centered finite volume method and block-structured grids. For the computation of the convective fluxes, the flux-difference AUSMDV Riemann solver is used. For what concerns the computation of the viscous fluxes, the gradients of the variables at cell interfaces are determined using the divergence theorem. The computations presented here are steady state analyses so that time plays the role of an iteration parameter to achieve asymptotically stationary flow in the compu-

tation. The numerical methods employed are a Runge-Kutta fifth-order explicit scheme and an implicit first order Euler scheme. The two methods are combined for obtaining a stable and efficient computation.

SSG/LRR-ω model

The Reynolds Stress Model (RSM) chosen to be implemented in QUADFLOW is the SSG/LRR-ω model form Eisfeld et al. (2005). This model is the combination of the SSG model form Speziale et al. (1991) in the far field and the LRR model from Launder et al. (1975) near the wall. The idea is to extend the applicability of the SSG model to wall-bounded flows in conjunction with an ω-equation. The LRR model chosen is a simplified version by Wilcox who coupled it with his ω-equation as in Wilcox (1993). The choice of this model near the wall is justified by the desire of having a low-Reynolds number model allowing integration up to the wall. As Wilcox shows, the near-wall behaviour of second-order closure models is strongly influenced by the scale-determining equation (Wilcox (1993)). Models based on an ω-equation often predict acceptable values of the wall integration constant and are quite easy to integrate through the viscous sublayer with respect to models based on the ϵ-equation. The ω-equation of Menter has been chosen to provide a turbulent length scale for the present model. The blending function of Menter has been employed to smoothly blend the coefficients of the two models.

The general equation describing the Reynolds stresses reads as follow:

$$\frac{\partial}{\partial t}(\bar{\rho}\tilde{R}_{ij}) + \frac{\partial}{\partial x_k}(\bar{\rho}\tilde{U}_k\tilde{R}_{ij}) = \tag{1}$$

$$\bar{\rho}P_{ij} + \bar{\rho}\Pi_{ij} - \bar{\rho}\epsilon_{ij} + \bar{\rho}D_{ij} + \bar{\rho}M_{ij} \quad .$$

The terms that appear at the right hand side of the equation represent the production, the redistribution, the destruction, the diffusion and the contribution of the turbulent mass flux, respectively.

Apart from the production term, which does not need modeling because it only depends on quantities for which an equation is solved, all other terms need to be modeled.

The re-distribution term is modeled as follows

$$\bar{\rho}\Pi_{ij} = -(C_1\bar{\rho}\epsilon + \frac{1}{2}C_1^*\bar{\rho}P_{kk})\tilde{b}_{ij} \tag{2}$$

$$+C_2\bar{\rho}\epsilon(\tilde{b}_{ik}\tilde{b}_{kj} - \frac{1}{3}\tilde{b}_{mn}\tilde{b}_{mn}\delta_{ij})$$

$$+(C_3 - C_3^*\sqrt{II})\bar{\rho}\tilde{k}\tilde{S}_{ij}^*$$

$$+C_4\bar{\rho}\tilde{k}(\tilde{b}_{ik}\tilde{S}_{jk} + \tilde{b}_{jk}\tilde{S}_{ik} - \frac{2}{3}\tilde{b}_{mn}\tilde{S}_{mn}\delta_{ij})$$

$$+C_5\bar{\rho}\tilde{k}(\tilde{b}_{ik}\tilde{W}_{jk} + \tilde{b}_{jk}\tilde{W}_{ik}) \quad ,$$

where all the coefficients are obtained inserting the values in Table (1) in the blending function (13) described below. In the above equation $\tilde{k}$ is the turbulent kinetic energy and ϵ is the specific dissipation. The tensors appearing in equation (2) are the anisotropy tensor

$$\tilde{b}_{ij} = \frac{\tilde{R}_{ij}}{2\tilde{k}} - \frac{\delta_{ij}}{3} \quad , \tag{3}$$

and II its second invariant, the strain rate tensor

$$\tilde{S}_{ij} = \frac{1}{2}\left(\frac{\partial\tilde{U}_i}{\partial x_j} + \frac{\partial\tilde{U}_j}{\partial x_i}\right) \quad , \tag{4}$$

the rotation tensor

$$\tilde{W}_{ij} = \frac{1}{2}\left(\frac{\partial\tilde{U}_i}{\partial x_j} - \frac{\partial\tilde{U}_j}{\partial x_i}\right) \tag{5}$$

and the traceless strain rate tensor $\tilde{S}_{ij}^*$.

Table 1: Coefficients of SSG and LRR model for the re-distribution term.

	C_1	C_1^*	C_2	C_3	C_3^*	C_4	C_5
SSG	3.4	1.8	4.2	0.8	1.3	1.25	0.4
LRR	3.6	0	0	0.8	0	2.0	1.11

The isotropic destruction term reads:

$$\bar{\rho}\epsilon_{ij} = \frac{2}{3}C_\mu\bar{\rho}\tilde{k}\omega\delta_{ij} \quad . \tag{6}$$

For what concerns the diffusion term the generalized gradient diffusion model is chosen:

$$\bar{\rho}D_{ij} = \frac{\partial}{\partial x_k}\left[\left(\bar{\mu}\delta_{kl} + D^{(GGD)}\frac{\rho}{\omega}\tilde{R}_{kl}\right)\frac{\partial\tilde{R}_{ij}}{\partial x_l}\right] . \tag{7}$$

The value of the constant $D^{(GGD)}$ is computed by the equation:

$$D^{(GGD)} = F\sigma^* + (1-F)\frac{C_s}{C_\mu} \quad . \tag{8}$$

F is the blending equation in (13), σ^*= 0.5 and C_s=0.22.

Finally the term $\bar{\rho}M_{ij}$ is neglected.

The Menter ω-equation for RSM reads as follows:

$$\frac{\partial}{\partial t}(\bar{\rho}\omega) + \frac{\partial}{\partial x_k}(\bar{\rho}\tilde{U}_k\omega) = \tag{9}$$

$$\bar{\rho}P^\omega - \bar{\rho}D^\omega + \frac{\partial}{\partial x_k}\left[\left(\bar{\mu} + \sigma_\omega\frac{\bar{\rho}\tilde{k}}{\omega}\right)\frac{\partial\omega}{\partial x_k}\right] + \bar{\rho}C_D$$

with the production term

$$\bar{\rho}P^\omega = -\alpha_\omega\frac{\omega}{k}\tilde{R}_{ik}\frac{\partial\tilde{U}_i}{\partial x_k} \quad , \tag{10}$$

the destruction term

$$\bar{\rho}D^\omega = \beta_\omega\bar{\rho}\omega^2 \tag{11}$$

and the cross-diffusion term

$$\bar{\rho}C_D = \sigma_d \frac{\bar{\rho}}{\omega} \max\left(\frac{\partial \tilde{\mathrm{k}}}{\partial \mathrm{x_k}} \frac{\partial \omega}{\partial \mathrm{x_k}}; 0\right) \quad . \tag{12}$$

The coefficients of the ω-equation as well as those of the Reynolds stresses are blended using the following function:

$$\phi = F\phi^{LRR} + (1-F)\phi^{SSG} \tag{13}$$

Table 2: Coefficients for ω-equation [9].

	α_ω	β_ω	σ_ω	σ_d
SSG	0.44	0.0828	0.856	$2\sigma_\omega$
LRR	0.5556	0.75	0.5	0

The coefficients for the ω-equation are listed in table 2. The blending function of Menter is defined as:

$$F = \tanh(\zeta^4) \tag{14}$$

with

$$\zeta = \min\left[\max\left(\frac{\sqrt{\tilde{\mathrm{k}}}}{\mathrm{C}_\mu \omega \mathrm{d}}; \frac{500\bar{\mu}}{\bar{\rho}\omega \mathrm{d}^2}\right); \frac{4\sigma_\omega^{(\mathrm{SSG})}\bar{\rho}\tilde{\mathrm{k}}}{\bar{\rho}\mathrm{C}_\mathrm{D}^{(\mathrm{SSG})}\mathrm{d}^2}\right]. \tag{15}$$

4 Preliminary Results

The results obtained from the first shots with a ramp angle of 40 degrees are presented here and compared with numerical results using the Reynolds stress model. The computational grid has 800x200 grid points and a wall resolution of 10^{-6} m. This grid resolution has been chosen since it allow to have almost square cells in the freestream. The numerical solution is stopped once the residual of density drops below 10^{-4}. For this test case a better convergence cannot be achieved due to unsteadiness in the simulated flow especially in the separated region. This unsteadiness is captured also in the experiment and show a small oscillation of the separation bubble over the test time. Figure 3 shows the Mach number distribution in the computational domain. The boundary layer separation is clearly visible at the end of the flat plate and a small region of subsonic flow is produced after the shock at the kink.

Inflow Conditions

The inflow conditions for the numerical simulations are derived by the conditions at the exit of the nozzle in the experiment. Table 3 presents the freestream conditions used here. The gas is considered as perfect gas with an isoentropic coefficient γ equal to 1.4.

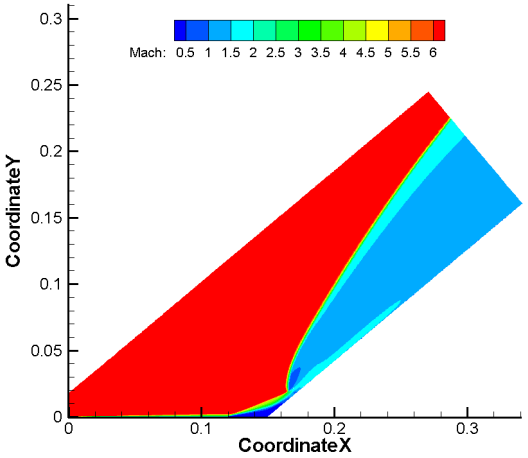

Figure 3: Mach number distribution in the computational domain.

Table 3: Free-stream conditions.

P_∞	9871 [KPa]
ρ_∞	0.08624 [Kg/m^3]
U_∞	2516 [m/s]
T_∞	390 [K]
M_∞	6.35 [-]

Boundary Condition

For what concerns the turbulent variables a turbulent intensity of 0.5% is chosen. At the supersonic inflow boundaries, the values are set equal to the freestram values. At the supersonic outflow boundaries, the flow variables are extrapolated from inside the domain.
At the solid wall the no-slip condition is imposed for the velocity components and for the Reynolds stresses. For the ω-equation, the Menter approach is chosen at the wall with constant wall temperature, in our case T_w=300 K.

Results

Figure 4 reproduce the experimental and numerical pressure distribution along the compression corner. It can be noticed that the first pressure value is higher than the turbulent attached value predicted by the simulation. From the time evolution of the pressure in that location it can be seen that the separation bubble is oscillating so that the thin film gauge in that position experiences both attached and separated flow as in Figure 5. The test time is considered to be between 6.5 and 8.5 microseconds. The second pressure value shows that the flow has separated as it also had in the numerical simulations. Further values along the compression ramp are in good agreement with the nu-

merical simulation.

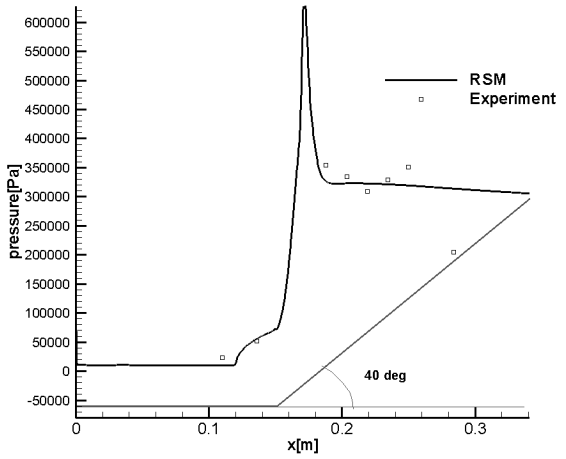

Figure 4: Pressure distribution along the 40 degrees compression corner

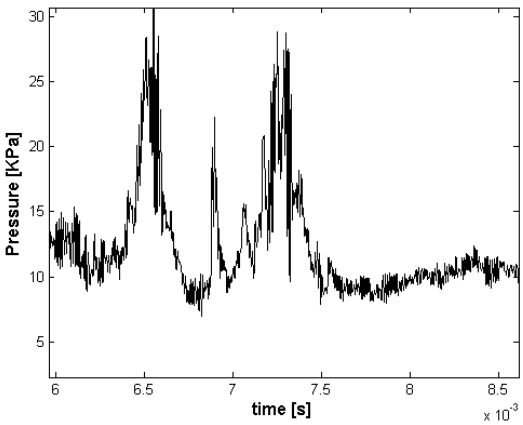

Figure 5: Time evolution of pressure for the first kulite.

For what concerns the heat fluxes, the values in the separation bubble are shown in figure 6. The second value corresponds to the same position as the first pressure value with respect to the distance from the leading edge. Also here it can be noticed that the value is higher than the one numerically predicted. Looking at the time evolution of the heat fluxes it can be seen that the flow turns from separated to attached along the test time, revealing an oscillation of the separation point as in Figure 7. Furthermore the comparison shows that the numerical simulation underestimate the size of the separation bubble and consequently the correct location of the separation.

5 Conclusions

The preliminary results shown here reveal a general good agreement between the computational and

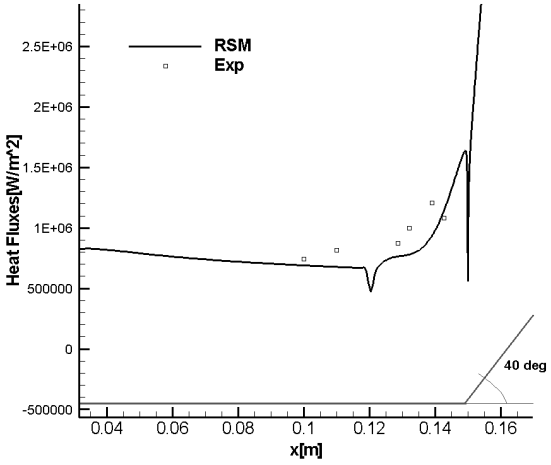

Figure 6: Heat fluxes distribution along the separation region.

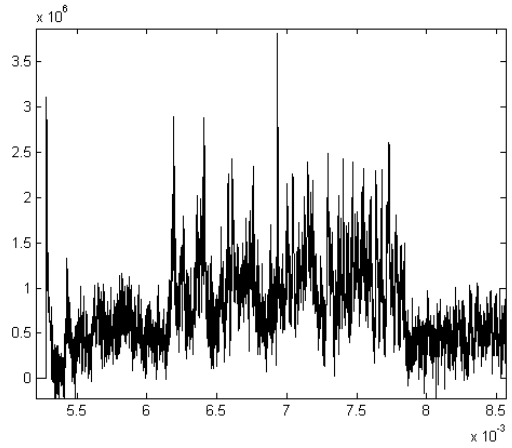

Figure 7: Time evolution of heat fluxes for the second thin film gauge.

the experimental data. An improvement in the agreement can be achieved by forcing the simulated flow to undergo a laminar to turbulent transition at the same location where the boundary layer trip is placed on the model. The differences in the heat fluxes values along the separation bubble suggests that the separation size is larger in the experiments than in the simulation, potentially because of non uniformities in the inflow conditions. This can be tested once the results of the pitot survey will be properly analyzed. Furthermore it has been noticed that the steady state numerical simulation is not able to account for unsteady phenomena like the small oscillation of the separation point even though the impossibility to drop the residuals below a certain level let us know that the flow under consideration is quasi-steady. For this kind of simulation a particular care should be taken while considering the results in 'transition'-regions like separation or reattachment where unsteady phenomena are more likely

to occur. A further comparison with other turbulence models like 2-equations models is required to assess whether the use of a 7-equation model is justified by an improvement in the prediction of the flow characteristics. In the next weeks the experiment moves to the 15 degrees compression corner and a further and more detailed analysis of the results, including also the heat transfer along the compression ramp will be conducted. Results from the flat plate using using sensors closer to the leading edge should show the correct position of the laminar to turbulent transition and allow a better set up of the numerical simulation.

Acknowledgments

Financial support from the Deutsche Forschungsgemeinschaft (German Research Association) through grant GSC 111 and Research Training Group GRK 1095 is gratefully acknowledged. A big thanks to James Turner for his invaluable help through all the experimental campaign.

References

Roy, C.J. and Blottner, F.G. (2006), Review and assessment of turbulence models for hypersonic flows, *Progress in Aerospace Sciences*, Vol. 42, pp. 469-530.

Olsen, M.E., Lillard, R.P. and Coakley,T.J. (2005), The Lag Model Applied to High Speed Flows, NAS Technical Report - NAS 05-005

Launder, B.R., Reece, G.J. and Rodi, W. (1975), Progress in the development of a Reynolds-stress turbulence closure, *J. Fluid Mech.*, Vol. 68, pp. 537-566.

Speziale C.G., Sarkar, S. and Gatski, T.B. (1991), Modelling the pressure-strain correlation of turbulence: an invariant dynamical system approach, *J. Fluid Mech.*, Vol. 227, pp. 254-272.

Eisfeld, B. and Brodersen, O. (2005) Advanced Turbulence Modelling and Stress Analysis for the DFG-F5 Configuration, 23^{rd} AIAA Applied Aerodynamics Conference, Toronto 6-9 June 2005.

Bramkamp, F., Lamby Ph. and Müller, S. (2004), An adaptive multiscale finite volume solver for unsteady and steady state flow computations, *J. Comp. Physics*, Vol. 197, pp. 460-490.

Mee, D., (2002), Boundary-Layer Transition Measurements in Hypervelocity Flows in a Shock Tunnel, *AIAA J.* 0001-1452, vol. 40 no. 8, pp. 1542-1548.

Krek, R.M. and Jacobs, P.A., (1993), Shock tube and nozzle calculations for equilibrium air, Technical report, The University of Queensland, Report No. 2/93, 1993.

Bosco A., Reinartz B. and Müller, S. (2009), Differential Reynolds Stress Model and grid adaptation for hypersonic double wedge simulations, Turbulence, Heat and Mass Transfer Conference, Rome 14-18 September 2009.

Wilcox, D.C. (1993), Turbulence Modeling for CFD, DCW Industries Inc.

Smith, A.L., (1993) Multiple component force measurement in short duration test flows, PhD Thesis, Department of Mechanical Engineering, The University of Queensland.